Characterization of similar Marshak waves observed at the LMJ

C Courtois, R. Gisbert, R Botrel, A Chaleil, L Chopineau, S Debesset, J Fariaut, O Henry, L Le Déroff, B Loupias, et al.

Characterization of similar Marshak waves observed at the LMJ

C. Courtois,[1,a)] R. Gisbert,[1] R. Botrel,[2] A. Chaleil,[1] L. Chopineau,[1] S. Debesset,[3] J. Fariaut,[1] O. Henry,[3] L. Le Déroff,[3] B. Loupias,[1] A. Rousseau,[1] G. Soullie,[1] B. Villette[1]

[1]*CEA, DAM, DIF, F-91297 Arpajon, France*

[2]*CEA, DAM, VALDUC, F-21120 Is sur Tille, France*

[3]*CEA, DAM, CESTA, F-33114 Le Barp, France*

[a)]Author to whom correspondence should be addressed: cedric.courtois@cea.fr

We detail results of two experiments performed at the Laser Mégajoule (LMJ) facility aimed at studying similar supersonic Marshak waves propagating in a low-density SiO_2 aerogel enclosed in metallic tubes. Similar means here that these two experiments, driven by the same input radiation temperature history, use purposely very different tubes in term of length (L = 1200 µm or 2000 µm), diameter ($2R$ = 1000 µm or 2000 µm), nature of the wall (gold or copper) and aerogel densities (ρ = 30 mg/cm^3 or 20 mg/cm^3), yet the transit time and the radiation temperature of the fronts at the tube exit are the same for both shots. Marshak waves are characterized at the exit using simultaneously for the first time to our knowledge, a one dimensional soft x-ray imager from which the radiation front transit time and curvature are measured and also a broadband x-ray spectrometer to infer its temperature history. These constraining results are then successfully compared to those from simple analytical models [A.P. Cohen et al., Phys. Rev. Research **2**, 023007 (2020) and O. A. Hurricane et al., Phys. Plasmas **13**, 113303 (2006)] and from the three dimensional Lagrangian radiation-hydrodynamics code TROLL to get information on x-ray energy losses. Controlled compensation effects between the length, diameter and nature of the tubes (governing these losses) are such that the radiation temperature drop along the tubes is eventually the same for these two similar shots.

I. INTRODUCTION

The contribution of radiation transfer in the evolution of astrophysical objects can play an important role.[1] This is particularly the case for instance with X-ray buster, when an accreting neutron star explodes in a binary system. The sudden release of x-ray energy interacts on a short period (tens of second for Type I burst) with the surrounding accretion disk that can then be altered.[2] The relative importance of radiation effects in these objects can be quantified by comparing the radiation energy density and the radiation flux to the corresponding material quantities.[3] The Boltzmann, $B_o = \rho e(\rho,T)v/F_{rad}(T)$, and the Mihalas, $R = \rho e(\rho,T)/E_{rad}(T)$, numbers can be introduced and should be below unit for systems where radiation dominates the energy transport and the medium internal energy density. The specific internal energy, function of the density, ρ, and temperature, T, is noted, e, here, $v \sim c_s$, corresponds to a characteristic fluid velocity that can be approximated by the sound velocity, c_s, and F_{rad} and $E_{rad}(T)$ are the radiation flux and the radiation energy density respectively.

High-power laser beams have already been used for years to produce intense radiation environments suitable to study systems where energy transport is dominated by radiation. Past experiments showed that laser energy deposition in millimeter scale gold cavities, gives access to radiation temperatures above 300 eV.[4] Even if these laboratory produced temperatures are not high enough to reach a regime where the radiation energy density dominates the medium internal energy ($R < 1$ would require radiation temperature above 1 keV, especially if one considers material density, ρ, large enough for the radiation transfer to be diffusive), Boltzmann number values below unit are on the contrary accessible.[5] As $B_o \propto R\, c_s/c$ where $c >> c_s$ is the speed of light, this simply underlines the efficiency of x-ray photons to transfer power in these systems compared for instance to the more classical contribution of electron or ion conduction. In another word, despite the radiation energy is negligible, the heat conduction is still through radiation due to absorption and black body emission from the matter, i.e., radiation flux

dominates, and material conduction is negligible comparing to the radiation heat conduction. In the particular case where the radiation front velocity is larger than the sound velocity, the front is said to be supersonic and can be characterized by a radiative Mach number $M_{rad}(t) = \partial_t z_F(t)/c_s(t) > 1$ where z_F corresponds to the front position. This regime of radiation transfer is particularly interesting as the density of the material heated by the radiation wave can be assumed constant, which greatly simplifies the equations of hydrodynamics.[6] Thus, this allows comparisons between results from simple analytical models and experiments.[7,8] These models often assume that the radiation transfer is diffusive and that the material Rosseland mean opacity, κ, and internal energy, e, are function of its density, ρ, and temperature, T, that can be approximated by, $e = fT^{\beta}\rho^{-\mu}$ and $1/\kappa = gT^{\alpha}\rho^{-\lambda}$,[9] where T is expressed in heV (1 heV = 100 eV), ρ in g/cm^3, f ~ 8.77 MJ/g, β ~ 1.1, μ ~ 0.09, g ~ 1/9175 g/cm^2, α ~ 3.53, λ = 0.75 for SiO_2 aerogel used in this study.[8] In the particular case where the radiation temperature drive is constant, and in a one-dimension (1D) approximation of the problem, $M_{rad} \propto T^{2+\alpha/2-\beta}\rho^{\lambda/2-1-\mu}t^{-0.5}$ showing the decrease of the supersonic Marshak wave velocity with time and the interest to use low density material such as foam and aerogel, to reach this particular radiative and supersonic regime.[10] Note that the medium density should not be too low for the diffusion-approximation to be valid, that is to assume that the x-ray photon mean free path is smaller than the typical temperature gradient length. Thus a minimum aerogel density, $\rho_{DA}(t) = [gf/(\sigma t)]^{1/(\mu+\lambda)}T^{(4-\alpha-\beta)/(\mu+\lambda)}$,[10] can be introduced (DA as "diffusion approximation") where $\sigma = 1.03\times10^{-2}$ MJ/ns/cm^2 is the Stefan-Boltzmann constant. In the conditions of the experiment described in this paper, ρ_{DA} ~ 20 mg/cm^3. On the other side, the use of a too high medium density leads to a regime of subsonic ($M < 1$) radiation transfer with the formation of a shock, or for intermediate densities, to the production of growing density perturbations with time for the transient transonic regime ($1 < M < 3$).[11-13] Beyond $M > 3$, radiation transfer can be considered as "clearly" supersonic, that is characterized by small density perturbations at the front, below

10% of the nominal material density. A density, ρ_{HS}, above which $\partial_t z_F(\rho=\rho_{HS\text{-}Mrad}) < M_{rad} \times c_0$ can be introduced and can be written as $\rho_{HS\text{-}Mrad}(t) = [4\Gamma g\sigma/[M_{rad}^2(12+3\alpha)r(1-\mu)f^2t]]^{1/(2-2\mu+\lambda)}T^{(4-2\beta+\alpha)/(2-2\mu+\lambda)}$,[10] where $\Gamma = 2+3\omega+(10/3)\omega^2+(251/72)\omega^3$, $\omega = \beta/(4+\alpha)$, T is again expressed in heV and t is time in ns. In our experimental conditions, $\rho_{HS\text{-}Mrad} \sim 90$ mg/cm^3 for $M_{rad} = 3$. Note that this density is optimistic as extracted from a simple 1D model. In reality, the density above which M_{rad} goes below 3 is lower than $\rho_{HS\text{-}Mrad}$ due to two dimensional (2D) effects.[7,8] The SiO_2 aerogel densities used in the LMJ experiment presented in this paper were then chosen at $\rho_0 \sim 20$ mg/cm^3 and $\rho_0 \sim 30$ mg/cm^3, to make sure the radiation front is well supersonic even if the diffusion approximation is less valid.

Several experiments using low-density material irradiated by soft x-ray source (photon energy < keV) have already been performed in the past and have employed different techniques to characterize supersonic Marshak wave. A promising one is based on 1D time resolved K-shell absorption spectroscopy to infer absolute plasma radiation temperature spatial profile at different discrete times.[11,14-19] That technique, that was actually mainly used for the moment for the transient transonic regime, requires the opacity of the low density material (foam or aerogel doped with Cl, Ti, used as a spectroscopy tracer) to be well known during data analysis,[18] and also requires several snapshots to get information on front dynamics. As this approach is based on spectroscopy absorption technique, the low-density medium is either free standing or enclosed in a low Z cylinder such as Be (with low wall albedo) so that energy leaks from the system can be important. Consequently, experiments dedicated to supersonic Marshak wave study generally use on the contrary, high-Z tube (gold) to maximize wall albedo and then to reduce wall x-ray energy losses.[20-26] These experiments are based on the measurement of the radiative wave self-emission using a soft x-ray imager or a broadband x-ray spectrometer. Early experiments used an imager coupled to a streak camera and pointed at the exit of the tube to continuously follow the time when the supersonic radiation front breaks through the edge of

the aerogel.[20-22] This experimental configuration also gives information on the front curvature, as the front propagates faster on-axis than near the walls because of 2D effects such as radiation energy losses at the wall tube (albedo, a, below unity).[7,8] Later, the dynamics of Marshak waves along tubes was studied more directly, on a single laser shot, by measuring self-emission through a longitudinal observation slit with 2D,[23-25] or 1D,[26] soft x-ray imagers. This type of measurement can be more constraining for analytical models or numerical simulations describing the dynamics of supersonic front, as it can be followed along the entire foam length and not only when it breaks through the edge. Yet, no direct information on the front curvature due to the energy losses is obtained. These losses can be indirectly studied by measuring the front radiation temperature history at the exit of the tube using a broadband x-ray spectrometer.[25] The drop of temperature between the exit of the tube and its entrance is due to several 2D effects acting as energy sink.[7,8] Note that in reference [25], no imager was used at the exit of the tube to study the front curvature.

In this paper, we present results of two similar shots performed at the Laser Mégajoule facility on the propagation of supersonic and moderately diffusive radiation fronts in a low-density SiO_2 aerogel enclosed in metallic tubes. Similar shots mean here that the two targets used the same drive temperature history but purposely very different tubes in term of length, diameter, nature of the tube wall and different aerogel densities, yet the design of this experiment is such that transit time and the temperature history of the radiation fronts at the exit of the tubes are the same for both shots, which highlights a control of x-ray energy losses. For the first time to our knowledge, simultaneous measurements of the front radiation temperature using a broadband x-ray spectrometer and of the front curvature using a 1D soft x-ray imager, are performed at the exit of the tube. These consistent and constraining results are then compared to those from simple analytical models,[7,8] and those from the three dimensional (3D) hydrodynamic simulations code TROLL to get information on x-ray

energy losses. Experimental setup is presented in section II and experimental results compared to the simple models in section III. Results from radiation hydrodynamic numerical simulations are presented in section IV before the conclusion.

II. EXPERIMENTAL SETUP

Experiments were performed at the CEA/CESTA using the Laser Mégajoule facility.[27] The experimental setup is presented in Fig. 1. Each target is constituted of a millimeter scale gold spherical cavity coupled to a metallic tube filled with a low-density silicon aerogel (SiO_2). Four quadruplets (Q28H, Q29H, Q28B and Q29B) delivering 40 kJ at 3ω (0.35 µm laser wavelength) in 3 ns (square pulse) heat the cavity. The incidence angle relative to the Laser Entrance Hole (LEH) normal is 60°, 41°, 46° and 57° respectively. The LEH normal points toward the angular position (90°,58.5°) of the LMJ experimental chamber. These quadruplets are focused at the centre of the LEH with gratings and are smoothed by combining longitudinal spectral dispersion and phase plates. The focal spot size is circular with the use of the LMJ D-type phase plates that produce circular spot that can be approximated by a super-Gaussian of order 2.7 and of 1020 µm diameter at 3% of the maximum intensity.

The metallic tube axis is at 90° relative to the LEH normal and then points toward the angular position (90°,148.5°) of the experimental chamber where the Systems for Insertion Diagnostic SID#12 is positioned. This SID#12 is equipped with the soft X-ray imager SSXI for this experiment. This article reports results of two of the shots performed during a radiation transfer campaign at the LMJ. Shot #1 uses a gold circular tube filled with a $2R$ = 1000 µm diameter, L = 1200 µm long SiO_2 aerogel at a density of $\rho = 29 \pm 0.5$ mg/cm^3 whereas Shot #2 uses a copper circular tube filled with a $2R$ = 2000 µm diameter, L = 2000 µm long SiO_2 aerogel at a density of $\rho = 18.9 \pm 0.15$ mg/cm^3. The pore size is below 1 µm. These effective densities are slightly different from those initially required by the design of the experiment (28 mg/cm^3

for Shot #1 and 20 mg/cm^3 for Shot #2) to get similar shots. Consequently, the transit time and radiation temperature history of the radiation waves at the exit of tube can exhibit slight discrepancies compared to the expectations for these two similar shots. The entrance of the tube is equipped with an aluminized mylar glint shield (e_{Al} = 50 nm, e_{Mylar} = 100 nm) to protect the aerogel against potential UV heating from the laser. The position z is defined in Fig. 1 and is along the tube axis. The position z = 0 corresponds to the beginning of the SiO_2 aerogel, on the spherical cavity side.

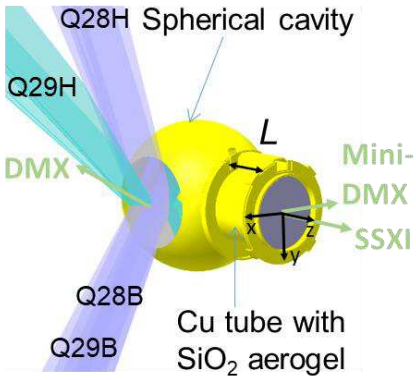

FIG. 1. Experimental setup showing the four LMJ quadruplets focused inside the spherical cavity equipped with the 2 mm diameter copper tube of Shot #2 containing the SiO_2 aerogel at a density of 19 mg/cm^3. The radiation temperature in the spherical cavity is inferred with the broadband X-ray spectrometer DMX. The Marshak wave is characterized at the exit of the tube using the soft X-ray imager SSXI and the broadband X-ray spectrometer Mini-DMX.

The spherical gold cavity radiation temperature history, T_R, is inferred from the time-resolved broadband x-ray spectrometer DMX which measures the x-ray flux from the LEH.[28] As DMX was located in port D9 for that experiment, at the position (70°,72°) of the

experimental chamber, the angle between the LEH normal and DMX axis is 24°. DMX is set up with the ten channels equipped with transmission filters and mirrors to select the soft part of the spectrum (< 1 keV) and ten others only equipped with transmission filters to study the hard part of the x-ray spectrum (> 1 keV).

A second broadband x-ray spectrometer called Mini-DMX, equipped with sixteen channels, eight dedicated to low photon energy (<1 keV) and eight to high photon energy (> 1 keV) is installed in the SID#26 located at (90°,180°) that is at 31.5° from the metallic tube axis. This diagnostic is used to measure the radiation temperature history of the supersonic front at the exit of the tube. A large protection cone (not represented in Fig. 1 for more clarity but represented in Fig. 6) mounted around the tube and pointing toward the SID#12, was glued on the spherical cavity to protect the tube from the laser energy contained in the focal spot at large radius (beyond the LEH). This cone is also used to make sure Mini-DMX only measures the x-ray signal coming from the exit of the tube and no emission from the spherical cavity.

The time-resolved 1D soft x-ray imager SSXI based on bi-toroidal mirror was then used in the SID#12, along the tube axis, to measure the supersonic radiation front self-emission at the exit of the tube. The mirror is coupled to a streak camera so that the front emission is continuously observed in the horizontal plan (x direction), along the tube diameter. The field of view of SSXI at the object plane is 5 mm yet, during this early experiment, this diagnostic was used in a preliminary configuration where the field of view was limited to 1 mm with also a reduced sensitivity at the edge. Consequently, Marshak waves were measured along the entire tube diameter of the tube for Shot #1, but only along a radius for Shot #2. The soft x-ray imager was filtered with a thin LEXAN foil coated with carbon corresponding to a photon energy measurement range of [150 eV - 284 eV], knowing the energy response of the streak camera.

III. EXPERIMENTAL RESULTS

A. CAVITY RADIATION TEMPERATURE

The cavity radiation temperature history, $T_R(t)$, inferred from DMX measurement for Shot #1 and Shot #2 is represented in Fig. 2. The measured maximum temperature is 178±3 eV for both shots that exhibit relatively similar time histories. The dashed line is a fit (used in section III-c) to the experimental data using the expression $T_R = T_0(t/t_0)^\delta$ with T_0 = 178 eV, t_0 = 3 ns and δ = 0.1. Dotted orange line corresponds to results for Shot #2 from TROLL numerical simulations presented in section IV.

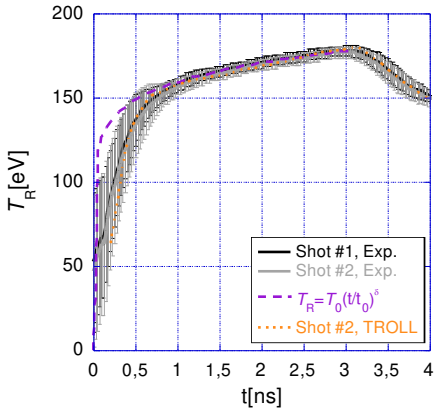

FIG. 2. Radiation temperature of the gold spherical cavity inferred from DMX measurement (solid lines) for Shot #1 (black line) and Shot #2 (gray line). The dashed line corresponds to a fit using the expression $T_R = T_0(t/t_0)^\delta$ with T_0 = 178 eV, t_0 = 3 ns and δ = 0.1. Results from TROLL numerical simulations are represented by the orange dotted line.

B. MARSHAK WAVE CURVATURE AND WALL ALBEDO

Figures 3(a) and (b) show images obtained with the soft x-ray imager SSXI for Shot #1 and Shot #2 respectively. The curvature of the supersonic radiation front at the exit of the tube is clearly visible. This phenomenon has already been observed in multiple experiments,[20-22,26] and is explained as the effect of x-ray energy losses at the tube wall due to limited albedo, $a <$

1,[7] that slows down x-ray propagation near the wall compared to on-axis propagation which ultimately curves the radiation front.

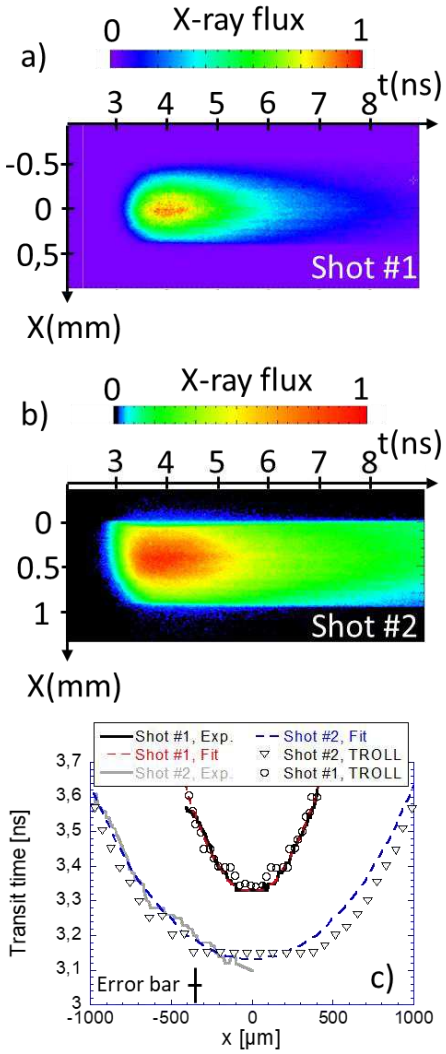

FIG. 3. (a) and (b) Results from the 1D soft x-ray imager SSXI showing the supersonic radiation front self-emission measured at the exit of the tube as a function of time for Shot #1 and Shot #2 respectively. (c) Measured (solid lines) transit time of the supersonic radiation

front at the exit of the tube as a function of the x transverse position. The cross shows the representative time and space error bars. Dashed lines correspond to fit described in the text. Results from TROLL simulations are represented by symbols.

The signal clip near position x = 0.5 mm in Fig. 3(a) and near positions x = 0 and x = 1 in Fig. 3(b) is due to the imaging mirror inside SSXI in its early version. The reduced sensitivity at the edge of SSXI field of view also explains the signal drop near position x = 0 for Shot #2. The transit time of the radiation front at the exit of the tube can be determined for different x positions along the tube diameter from inflection points extracted from temporal profiles. This transit time is represented by solid lines in Fig. 3(c) for both shots. The radiation front on-axis breakthrough time at the edge of the aerogel is 3.35±0.05 ns for Shot #1 and 3.10±0.05 ns for Shot #2. As expected, these times are relatively close for these two similar shots. The slight on-axis discrepancy of 250 ps could be explained by the effective densities of the aerogel used inside the tubes that are not those initially required by the design of that experiment to get similar shots. For Shot #1, the transit time should have been slightly earlier with the initial lower value required (28 mg/cm^3 instead of 29 mg/cm^3 obtained) whereas for Shot #2, the larger density required (20 mg/cm^3 instead of 18.9 mg/cm^3 obtained) would have slowed down the radiation front, reducing the delay between the two transit times.

The model in reference [7] describes bent Marshak waves propagating in low-density material by x-ray energy losses at the tube wall containing the aerogel. This model assumes that material Rosseland mean opacity, κ, internal energy, e, are function of its density, ρ, and temperature, T, so that, as already discussed, they can be approximated by, $e = fT^{\beta}\rho^{-\mu}$ and $1/\kappa = gT^{\alpha}\rho^{-\lambda}$ (see the introduction part). From reference [7], the transit time can be expressed as a function of the transverse position, at the longitudinal position corresponding to the exit of the tube, $z = L$. In cylindrical coordinates relevant to a tube, this time can be written as: [26]

$$t = \left\{ \frac{(1+4\delta)R^2}{D\epsilon t_0^{-4\delta}} \left[cosh\left(\frac{\sqrt{2\varepsilon}}{R} \frac{L}{J_0\left(\frac{r\sqrt{2\varepsilon}}{R}\right)} \right) - 1 \right] \right\}^{1/1+4\delta}, \qquad (1)$$

where $r = (x^2+y^2)^{1/2}$ is the transverse position (perpendicular to the radiation wave propagation direction z) in cylindrical coordinate, R is the tube radius, ε is a dimensionless small (<1) parameter related to the wall albedo, a, by $\varepsilon = (3/4)\kappa\rho R(1-a)$. J_0 is the Bessel function of the first kind of order zero. $D = D_M(1+\varepsilon/2)$ is a modified radiation diffusion constant, where $D_M = 8\sigma T^4/(3\kappa\rho e)$ is the diffusion constant of Marshak wave and $\sigma = 1.03\times10^{-2}$ MJ/ns/cm^2. In our experimental conditions, $t_0 = 3$ ns and $\delta = 0.1$ are the parameters used in the expression of $T_R = T_0(t/t_0)^\delta$ that approximates the radiation temperature history at the entrance of the tube [see Fig. 2]. Yet, as already discussed in reference [8], the entrance of the tube is affected by radiation closure due to the intense x-ray emission from the spherical cavity that is at the origin of an expansion of the wall, within 100 µm typically. As the experimental conditions discussed in reference [8] are similar to ours in term of temperature, the effective input x-ray flux drive should be multiplied by a transmission coefficient of 0.64 for Shot #1 because of the reduction of the 1 mm diameter tube entrance surface and by a larger transmission coefficient of 0.81 for Shot #2 because of the larger diameter. Consequently, the drive radiation temperature history at the entrance of the tube is set as $T_D = K \times T_R$ in the present model with $T_D = 0.9 \times T_R$ for Shot #1 and $T_D = 0.95 \times T_R$ for Shot #2. As the SiO_2 aerogel used in this experiment has a relatively low density, the Rosseland mean free path, $\lambda_{Ross} = 1/(\kappa\rho)$ can be larger than the tube diameter $2R$, especially at the entrance of the tube where the radiation temperature is the highest. For Shot #2, $\lambda_{Ross} \sim 4$ mm with $\rho = 29$ mg/cm^3 and $T_0 = 1.78$ heV. Consequently, x-ray photon can interact with the tube within a Rosseland (material) mean free path reducing the effective path.[29,30] An effective x-ray photon mean free path, λ_{eff}, should then be introduced to take into

account the geometry of the experiment. Using a harmonic average,[30] it can be written $1/\lambda_{eff} = 1/\lambda_{Ross} + 1/\lambda_{geom}$ where $\lambda_{geom} = 2R$ is the geometric photon mean free path. This harmonic average makes sure that the effective mean free path is shorter than the tube diameter at the entrance of the tube, where the radiation temperature is high. At the exit, where the temperature is lower, $\lambda_{eff} \sim \lambda_{Ross}$. An effective opacity can then also be introduced as $\kappa_{eff} = 1/(\lambda_{eff}\rho)$ and should be used in the above expressions of the modified radiation diffusion constant D_M and ε to take into account x-ray photon mean free path reduction due to the presence of the tube wall. Dashed lines of Fig. 3(c) are fits to the measured transit time using Eq. (1) from which the parameters ε and D can be determined. For Shot #1, one gets $\varepsilon = 0.16\pm0,04$ and $D = 0,67\pm0,03$ mm²/ns using $T_D = 0.9 \times 1.78$ heV and $\rho = 2.9\times10^{-2}$ g/cm² and $\varepsilon = 0.18\pm0.03$ and $D = 1,98\pm0.06$ mm²/ns for Shot #2 with $T_D = 0.95 \times 1.78$ heV and $\rho = 1.89\times10^{-2}$ g/cm². The larger value of the modified radiation diffusion constant for Shot #2 is mainly due to the lower SiO_2 aerogel density used for that shot which leads to higher radiation wave velocity. The wall albedo can then be determined from $\varepsilon = (3/4)\kappa_{eff}\rho R(1-a)$, one gets $a = 0,69\pm0.08$ for Shot #1 performed with the gold wall and $a = 0,62\pm0.07$ for Shot #2 performed with the copper wall. The value of the gold wall albedo is compatible with results presented in reference [31] where $a = 0.78$ is obtained for the same material (high-Z) at $T = 0.9 \times 1.78$ heV over 3 ns. Assuming the following relation,[32,33] $(1-a)/a = \dot{E}(t)/\sigma T_D{}^4$ between the wall albedo, a, and the total absorbed flux per unit area, $\dot{E}$, one can infer from this model and the above albedo values that this absorbed flux is ~ 1.6±0.1 larger in the copper wall than in the gold wall. Note that an assumption needed to apply the above model is that $2R\rho\kappa >> 1$ which is not fully obtained in our experimental conditions, as $2R\rho\kappa \sim 1.4$. Note that the model presented in reference [7] assumes that the effective drive temperature, T_D, should be known to infer the wall albedo from the small parameter ε. It is here simply obtained by introducing a convenient multiplication factor as routinely performed during post-shot modeling (either on the material opacity in reference [25],

on the laser power profile [34], or directly on the drive x-ray flux [35]), but to be more rigorous, more sophisticated models could be used to determine an effective source temperature. For instance, using the source temperature, T_S, defined in the next section from the model presented in reference [8], leads to a higher albedo value for the gold wall, $a = 0.76$, which is still within the error bars of the previous value inferred from a less rigorous, but common approach.

C. RADIATION TEMPERATURE AT THE EXIT OF THE TUBE AND X-RAY ENERGY LOSSES

An interesting quantity to measure during radiation transfer experiments is the emergent X-ray flux at the end of the tube as it is sensitive to energy loss mechanisms involved during the transfer.[8,36] The black solid lines of Fig. 4(a) and (b) represent the radiation temperature history at the exit of the tube for Shot #1 and Shot #2 respectively. These results are inferred from the broadband x-ray spectrometer Mini-DMX measurement. As expected by the design of that experiment, the maximum temperature is close for these two similar shots, $T_{out} = 92 \pm 3$ eV and $T_{out} = 90 \pm 3$ eV, and peaks at around t = 4 ns. This time is consistent with the maximum emission observed with the soft x-ray imager SSXI as shown in Fig. 3.

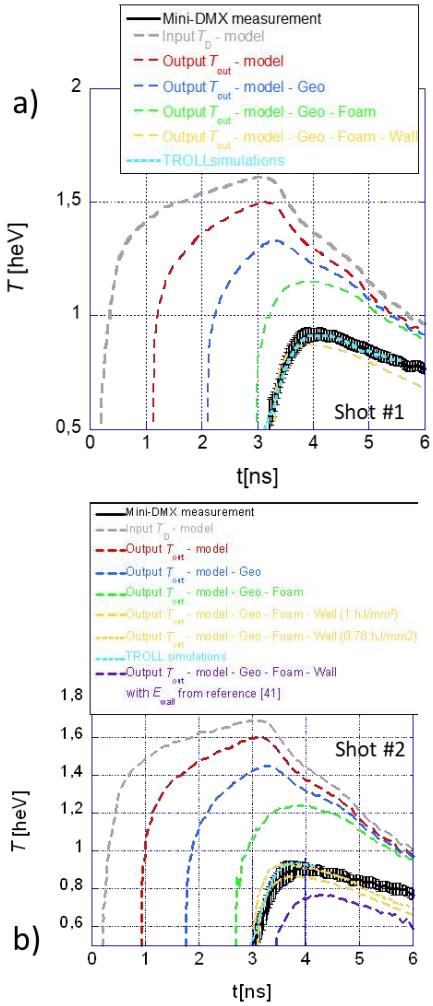

FIG. 4. Radiation temperature measured at the exit of the tube with the broadband X-ray spectrometer Mini-DMX (black solid line) for the two similar shots, Shot #1 (a) and Shot #2 (b). Dashed gray line is the input drive temperature at the entrance of the tube, T_D. The following colored dashed lines are results from the simple model discussed in this section successively improved by taking into account the effect on the output radiation temperature, of the geometry of the tube that reduces the effective photon mean free path, the energy stored

in the foam and the x-ray energy losses inside the tube wall. The purple dashed line is similar to the yellow lines but uses the expression $E_{wall}(t) = 1.58T_0^{3.4}[t - t_0(x)]^{0.61}$ from reference [41] introduced later in this section. Results from TROLL numerical simulations are represented by the cyan dotted lines.

The dynamic of supersonic and diffusive radiation waves propagating inside an aerogel is governed by x-ray photon emission and absorption processes. The radiation wave position, Z_F, can be expressed as a function of the input x-ray drive temperature, T_D, using a 1D model described in reference [9] and can be written as:

$$Z_F(t) = \left(\frac{2+\varepsilon}{1-\varepsilon} C H^{-\varepsilon}(t) \int_0^t H(t')dt'\right)^{1/2}, \qquad (2)$$

where $\varepsilon = \frac{\beta}{4+\alpha}$, $C = \frac{16}{4+\alpha}\frac{g\sigma}{3f\rho^{2-\mu+\lambda}}$ and $H(t) = T_D^{4+\alpha}(t)$. The parameters β, α, g, f, μ, λ were already introduced in Sec. III. B. As a reminder, T_D is defined as the input drive radiation temperature associated to the x-ray flux effectively entering the tube. Figures 5(a) and 5(b) compare the measured on-axis transit times of the radiation front determined from the soft x-ray imager SSXI [see Fig. 3(c)] to results obtained using Eq. 2 (red dashed lines) which are too early. The red dotted line in Fig. 5(a) is obtained from Eq. (3) determined by using $T_D = KT_0(t/t_0)^\delta$ in Eq. (2):

$$z_F^2 = \frac{16\left(2+\frac{\beta}{4+\alpha}\right)g\sigma\rho^{-2-\lambda+\mu}t^{1+\delta(4+\alpha-\beta)}t_0^{-\delta(4+\alpha-\beta)}K^{4+\alpha-\beta}T_0^{4+\alpha-\beta}}{3(4+\alpha)\left(1-\frac{\beta}{4+\alpha}\right)(1+(4+\alpha)\delta)f}. \quad (3)$$

Note that a similar expression has already been published by Malka et al. in reference [13]. For Shot #1, $KT_0 = 0.9 \times 1.78$ heV, $t_0 = 3$ ns and $\delta = 0.1$, the red dotted line is not superimposed with the dashed one but is rather parallel. This is due to the approximation of the DMX measured radiation temperature history by $T_0(t/t_0)^\delta$ which is not correct before t = 1 ns [see Fig.

(2)]. At late time, the dotted and the dash line converge towards the same limit, $z_F \propto t^{[1+\delta(4+\alpha-\beta)]/2} \sim t^{0.82}$.

As discussed in detail in reference [8], this significant difference between the red dashed line and the experimental results is due to physical phenomena, such as x-ray energy losses at the tube wall, the energy stored in the aerogel that are not included in the previous simple 1D model.

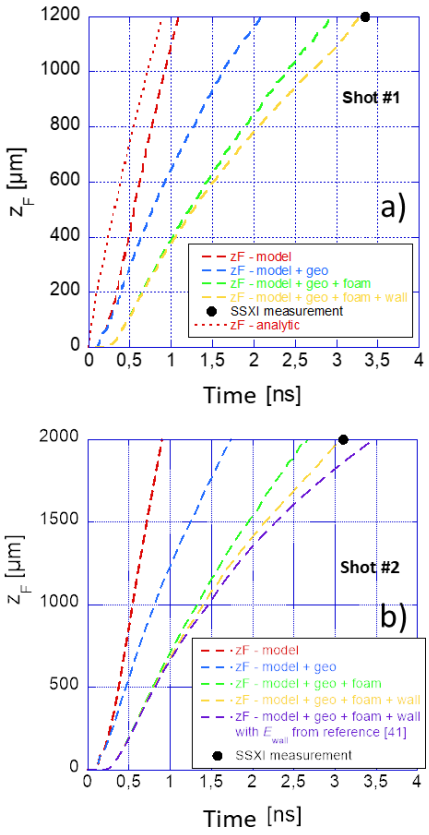

FIG. 5. Radiation front position, Z_F, as a function of time from the models described in references [9] (dashed red line) and [8] (other dashed lines) compared to the transit time measured with the soft x-ray imager SSXI (black points) for Shot #1 (a) and Shot #2 (b).

Results from the simple model are here successfully improved by taking into account the effect on radiation wave dynamics of the geometry of the tube that reduces the effective photon mean free path (blue), the energy stored in the foam (green) and the x-ray energy losses inside the tube wall (yellow). The purple dashed line is similar to the yellow one but uses the expression $E_{wall}(t) = 1.58T_0^{3.4}[t - t_0(x)]^{0.61}$ from reference [41] introduced later in this section. The red dotted line in Fig. 5(a) is obtained from Eq. (3).

A first improvement in our analysis, should be to include the already introduced effective opacity, $\kappa_{eff} = 1/(\lambda_{eff}\,\rho)$ with the effective x-ray photon mean free path, $1/\lambda_{eff} = 1/\lambda_{Ross} + 1/\lambda_{geom}$ and $\lambda_{geom} = 2R$, to take into account the geometry of the tube and the fact that at high radiation temperature, the Rosseland mean free path is larger than the diameter of the tube.[29,30] To do so, an effective parameter g_{eff} is introduced with $1/\kappa_{eff} = g_{eff}T^{\alpha}\rho^{-\lambda}$ and $g_{eff} = (\lambda_{eff}/\lambda_{Ross})g$. As a reminder g ~ 1/9175 g/cm^2 for SiO_2 aerogel. This effect is maximum at around t = 3 ns when the radiation temperature of the spherical cavity reaches its peak. At that time, the parameter g_{eff} drops by a factor 3.9 for Shot #1 and by a factor 4.6 for Shot #2 due to a smaller diameter tube. The blue dashed lines of Fig. 5(a) and 5(b) show the effect of the tube geometry on the radiation front that propagates about twice slower compared to results from the original simple 1D model (the time at which the front breaks through the aerogel increases by 86% for Shot #1 and by 92% for Shot #2). Yet experimental points are still later. Note that this shortening of the effective photon mean free path using a harmonic average is purely a geometric effect here as only λ_{Ross} and $\lambda_{geom} = 2R$ are used to determine λ_{eff}. In particular no information on the nature of the tube (Au or Cu), that governs x-ray energy leaks at the wall, is considered. These wall leaks are treated separately later in this section.

Another phenomenon that should be included to improve the model is the internal energy stored by the aerogel. This aspect has been discussed in detail in reference [8] and more recently

in reference [37]. The effective x-ray flux source feeding the entrance of the tube can be written $\sigma T_S^4(t) = \sigma T_D^4(t) - ½\, F(z=0,t)$ where as a reminder T_D is the input drive radiation temperature from the spherical cavity. F is a term corresponding to the heated aerogel reemission and can be determined from $F(z=0,t) = \dot{E_a}(t)$ where the total energy stored inside the aerogel can be written as $E_a(t) = f\rho^{1-\mu} z_F(t) H^{\epsilon}(t)(1-\varepsilon)$. The green dashed lines of Fig. 5 represent the radiation wave position inferred from the simple model taking into account the effective photon mean free path due to the geometry of the tube and the energy stored inside the aerogel. These results are obtained using the suggested algorithm found in reference [38]. The time when the front breaks through the edge of the aerogel is still early compared to the measurement. The position between the blue and the green lines increases by 44% for Shot #1 and by a slightly larger value of 50% for Shot#2, mainly due to a longer aerogel even if its density is lower.

Another important phenomenon discussed in reference [8] that reduces the velocity of the radiation wave propagating inside a tube is the x-ray energy lost inside the tube wall. For a constant boundary temperature, the energy lost per unit of surface can be written $E_{wall}(t) = kT_0^b[t - t_0(x)]^c$ where the energy is in hJ/mm^2 (1 hJ = 100 J). For gold, k = 0.59 hJ/mm², b = 3.35 and c = 0.59. The energy losses are estimated via a subsonic self-similar solution in the tube wall as these opaque and solid density cover materials of the foam, i.e. gold or copper, generate subsonic Marshak waves, when the energy stored in them. This expression is used for Shot #1 performed with the gold wall as the radiation temperature history is relatively constant in our experimental conditions (δ = 0.1). Radiation wave position as a function of time, including the tube geometry, the foam reemission and the wall energy losses effects, is represented by the yellow dashed line in Fig. 5(a) obtained again with the algorithm from reference [38]. A good agreement with the measurement, within the error bars, is obtained. For Shot #2, the energy lost in a copper wall is not expressed in reference [8], yet the coefficients b and c can be determined from reference [33] assuming again a constant boundary temperature.

The copper Rosseland mean opacity, κ, and internal energy, e, are again approximated by $e = fT^{\beta}\rho^{-\mu}$ and $1/\kappa = gT^{\alpha}\rho^{-\lambda}$,[9] where T is still expressed in heV (1 heV = 100 eV), ρ in g/cm^3, f ~ 5.7 MJ/g, β ~ 1.35, μ ~ 0.14, g ~ 4.47×10^{-4} g/cm^2, α ~ 2.21, λ = 0.29 from the copper SESAME equations of states and from reference [39] for the opacity terms. Using these values, one gets b = 3.40 and c = 0.61. The coefficient k is more difficult to determine, as it is not explicitly expressed in [33]. It is then fixed so that results from the above model are in agreement with the measurement as shown in Fig. 5(b). One gets then k = 1.00 hJ/mm² for copper. Yet, estimation of the total absorbed flux per unit area, $\dot{E}$, using this value of k shows that the flux in the copper wall is ~ 1.9 larger than in the gold wall which is a higher value compared to the estimation (~ 1.6) obtained from the radiation front curvature analysis presented in section III-b. A value of k = 0.78 hJ/mm^2 is needed to recover this x-ray flux ratio of 1.6 but the transit time (2.99 ns) is then shorter compared to the measurement, slightly outside the error bars. Since the transit time is not only sensitive to the wall energy losses but depends on other phenomena discussed above, it is likely a less relevant quantity to infer information on wall losses contrary to the approach based on the front curvature analysis. The model also indicates that the use of the nominal required aerogel densities indeed reduces the delay between the transit time of these two similar shots as it would be 3.17 ns for Shot #1 and 3.19 ns for Shot #2.

It is also interesting to evaluate the efficiency of radiation to transfer energy flux in this experiment by computing the Boltzmann number. It is B_0 ~ 0.05 for Shot #1 and B_0 ~ 0.07 for Shot #2 at the entrance of the tube and B_0 ~ 0.3 and B_0 ~ 0.4 at the exit showing that x-ray photons indeed mainly carry the energy flux inside the tube.

The measured (black solid lines) radiation temperature history from Mini-DMX at the exit of the tube, is compared to results from the above model (dashed lines) in Fig. 4. The output

radiation temperature is assumed to follow a Henyey-like profile [8] which is a good approximation for the temperature profile:

$$T_{Hy}(L,t) = T_S(t)\left(1 - \frac{L}{Z_F(t)}\right)^{1/1+4\delta}, \qquad (4)$$

where $T_S(t)$ and $Z_F(t)$ are determined from the above model. Note that more exact profiles could have been considered in this study [13,40]. The gray dashed line represents the input drive temperature $T_D(t)$ as a reference. The other colored dotted lines follow the convention of Fig. 5 in term of phenomena taken into account to describe the slowing down and the decrease of temperature of the radiation waves along the tube. The yellow line represents then the output radiation temperature taking into account the tube geometry, the energy stored in the foam and the wall effects on energy losses with k = 1.00 hJ/mm² (dashed line) or k = 0.78 hJ/mm² (dotted line) for copper. Figures 4 shows that the radiation temperature at the exit of the tube drops by a factor two compared to the input drive one, T_D. As expected, the exit radiation temperature is almost the same for both shots even if the length, the diameter and the nature of the walls are different.

A similar analysis as the one presented above but using the following expression [41] of the energy lost per unit of surface for copper, $E_{wall}(t) = 1.58T_0^{3.4}[t - t_0(x)]^{0.61}$, determined from self-similar subsonic results as in reference [33] leads to slightly different results. Because of a larger energy loss (larger value of the k parameter), the radiation temperature at the exit of the tube is lower, ~ 76 eV [see the purple dashed lines of Fig. 4(b)], and the radiation front transit time is also later by approximately 300 ps [see the purple dashed lines of Fig. 5(b)]. Note also that we did not use in this section the full model presented in reference [8] as a correction of the aerogel density could have also been introduced to take into account an increase of its density as it is compressed by the hydrodynamic ablation of the tube wall. This leads to a slightly slower radiation wave velocity.

To summarized this section, as the first shot uses a smaller tube diameter and a larger aerogel density than Shot #2, the radiation wave velocity is slower because of larger losses per unit area (that increases according to 1/R for a given wall material) and a shorter Rosseland photon mean free path due to the larger density and an even shorter effective photon mean free path due to the smaller tube diameter. Yet, the use of a shorter tube made of gold instead of copper for Shot #1 reduces the length to propagate to reach the exit of the tube and also reduces the wall x-ray energy losses because of the larger albedo. Eventually, the design of these two very different shots (different diameter, length, nature of the wall for the tube and different aerogel density filling the tube) is such that the radiation wave transit time and radiation temperature drop along the tubes are the same for these two similar shots.

IV. NUMERICAL SIMULATION RESULTS

The numerical simulations of this LMJ experiment were performed with the 3D (three-dimensional) Lagrangian radiation-hydrodynamics code TROLL used in the arbitrary lagrangian-eulerian (ALE) mode.[42] Tabulated EOS (Equation Of State) and OPALV opacity[43] tables are used. Radiation transport is handled with an implicit Monte-Carlo (IMC), multigroup method. These simulations were performed on the Tera-1000 supercomputer at CEA-DIF and required 512 processors over 100 h. Figure 6 shows a representation of the target used in the TROLL simulations for Shot #1. It is made of 2 million zones. The spherical cavity, the gold tube containing the SiO_2 aerogel and the protection cone can be seen, as well as the quadruplets used to heat the cavity and a representation of the lines of sight of the two broadband x-ray spectrometers DMX and Mini-DMX and the soft x-ray imager SSXI.

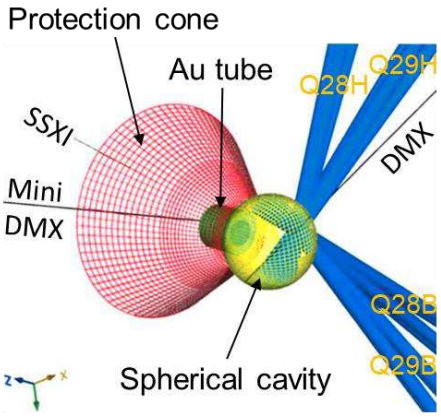

FIG. 6. 3D representation of the target used in TROLL simulation showing the spherical cavity with its protection cone and the gold tube used for Shot #1. The four quadruplets focused inside the spherical cavity and the lines of sight of the broadband X-ray spectrometers DMX, Mini-DMX and soft x-ray imager SSXI are also represented.

In a 3D radiation-hydrodynamics code, the real target geometry is considered without approximation often required with 2D simulations. Consequently, and as it will be shown in this section, the 3D simulations agree relatively well with the entire constraining set of experimental data (cavity radiation temperature, radiation front curvature, burnthrough time and time resolved temperature at the exit of the tube).

Similarly to the measured radiation temperature of the cavity, the simulated one is obtained by computing the incident x-ray flux (photon energy between 0 and 2 keV) from the LEH on a detector, knowing its distance and angular position relative to the LEH. This approach assumes that the LEH surface emits like a blackbody, the radiation temperature is then proportional to the ¼ root of the x-ray flux. The simulated radiation temperature of the cavity shown in Fig. 2 for Shot #2, is in agreement within the error bars with the measurements (no multiplier was used in the simulation).

Figure 7 represents the simulated signal of the soft x-ray imager SSXI for Shot #2. As for the experiment, the spatial axis corresponds to tube diameter along the x-axis. The energy response of SSXI is taken into account in the simulation of this image. The curvature of the radiation front is here also observed with the front breaking through the edge of the aerogel earlier on the tube axis. Similarly to experimental data, the numerical transit time of the radiation front at the exit of the tube is determined for different x positions along the tube diameter from inflection points extracted from temporal profiles. This simulated transit time is represented by the symbols in Fig. 3(c) (circles for Shot #1 with the 1 mm diameter gold tube and triangles for Shot #2 performed with the 2 mm diameter copper tube). The on-axis transit time is around 200 ps earlier for Shot #2 compared to Shot #1due to differences between the required (by the design) and effective experimental conditions. Numerical simulations performed with the nominal required conditions reduce the on-axis transit time difference between these two shots down to 100 ps.

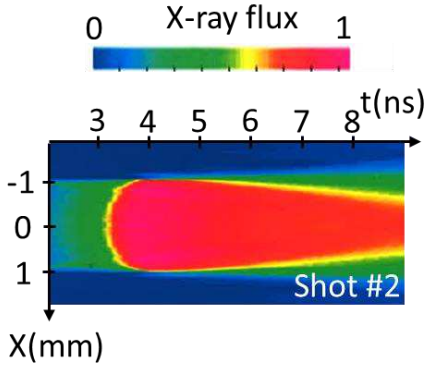

FIG. 7. Simulated signal from the soft x-ray imager SSXI for Shot #2 performed with the 2 mm diameter copper tube.

The simulated radiation temperature history at the exit of the tube is represented by the cyan dotted line in Fig. 4. As expected, the maximum temperature is almost identical for these two similar shots (91 eV for Shot #1 and 93 eV for Shot #2).

Figure 8(a) represents the simulated net cumulated x-ray energy entering the copper (black solid line) and the gold (gray solid line) tubes as a function of time. The larger cumulated energy for Shot #2 is simply due to the larger diameter of the copper tube ($2R$ = 2000 µm) compared to the gold one ($2R$ = 1000 µm). Note that the energy ratio between these two tubes is slightly larger than the expected factor 4, as the smaller diameter tube entrance is relatively more sensitive to radiation closure. The simulated cumulated absorbed energy, $E(t)$, by the copper (dashed black line) and the gold (dashed gray line) tube walls are also represented in Fig. 8(a). As expected, as the gold tube has a smaller diameter and also a shorter length, the absorbed energy by the gold wall is smaller than in the copper wall.

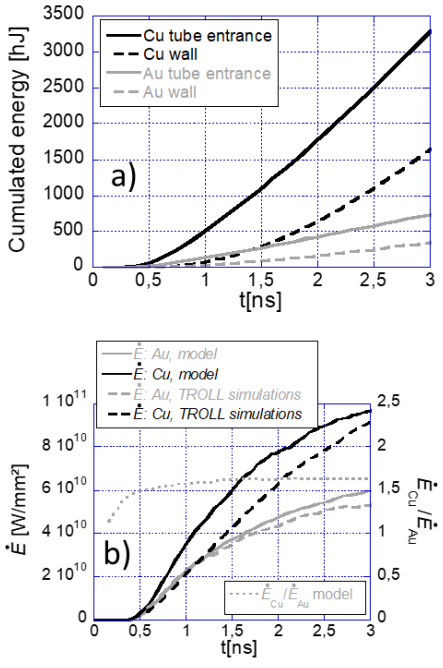

FIG. 8. (a) Simulated cumulated absorbed energy by the copper (black dashed line) and the gold (gray dashed line) tube walls and net cumulated energy entering the copper (black solid line) and gold (gray solid line) tubes. (b) Total absorbed flux per unit area in the copper (black line) and gold (gray line) wall from the model (solid line) and the TROLL simulation (dashed line). The grey dotted line represents the total absorbed flux per unit area ratio between the copper and gold walls from the model.

The simulated absorbed flux per unit area, $\dot{E}(t)$, in the copper (black dashed line) and gold (gray dashed line) walls are presented in Fig. 8(b). These quantities are averaged over the tube length. The solid lines are results from the model discussed in section III-c where the energy lost per unit of surface, $E_{wall}(t)$, was introduced. The solid line represents more precisely the time derivative of this energy loss, also averaged over the tube length. The ratio of this last quantity between the copper and the gold walls is represented by the dotted line that shows that the power losses inside the copper are as expected 1.6 more important than in gold. This is due to the chosen value of the parameter k = 0.78 hJ/mm^2 in the expression of $E_{wall}(t)$ for copper (see section III-c). A relatively good agreement is obtained between the simulated results and those from the model. This gives a qualitative explanation of the similar propagation between the two shots. The smaller tube radius, R_{Au}, used for Shot #1 performed with the gold wall, tends to increase the losses per unit surface area of the tube and also to reduce the effective x-ray photon mean free path, λ_{eff}. The radiation closure of the tube entrance is also expected to be more important leading to lower drive radiation temperature, T_D. Yet, this is compensated by the use of a tube 1.7 time shorter and a total absorbed flux per unit area 1.6 time smaller (same transit time) in gold than in copper so that the radiation temperature drop along the tubes is eventually the same for these two similar shots.

V. SUMMARY

The objective of this experiment performed on the Laser Mégajoule facility was to study the propagation of similar supersonic and moderately diffusive radiation waves in low-density SiO_2 aerogel in metallic tubes driven by thermal radiation from a laser-heated spherical cavity. These shots were designed so that the time when the radiation front breaks through the edge of the aerogel (the transit time) and the exit temperature history are the same even if they use on purpose very different tubes in term of length (L = 1200 µm or 2000 µm), diameter ($2R$ = 1000 µm or 2000 µm), nature of the tube wall (gold or copper) and different aerogel densities (ρ = 30 mg/cm^3 or 20 mg/cm^3). The radiation temperature is inferred from the broadband x-ray spectrometer Mini-DMX. The transit time is obtained from the soft x-ray imager SSXI from which the front curvature is also studied. Experimental results show that these two shots are, as expected, indeed similar even if slight variations of the effectively produced SiO2 aerogel density compared to the requirement (29±0.5 mg/cm^3 instead of 28 mg/cm^3 for Shot #1 and 18.9±0.15 mg/cm^3 instead of 20 mg/cm^3 for Shot #2) increase by ~100 ps the difference between the transit times.

Experimental results are then compared to those from the 3D (3 dimensional) Lagrangian radiation-hydrodynamics code TROLL and are found in good agreement. They are also compared to results from two simple analytical models describing energy losses during radiation wave propagation in tubes. A good agreement is found with the predictions from the Cohen et al. model [8,38] (where an effective x-ray photon mean free path, λ_{eff}, is used instead of the Rosseland mean free path) concerning the burnthrough time and the emitted flux of the Marshak wave. Concerning the bent shape of the Marshak wave, it is inferred from the Hurricane model [7] that the total absorbed flux per unit area, $\dot{E}$, is larger (×1.6) for the copper wall compared to the gold wall due to a lower albedo, a. The geometry of the tube of radius R and length L is here actually designed so that the use of a smaller diameter for Shot #1, that

increases the losses per unit surface area of the tube (according to $1/R$) and reduces the effective x-ray photon mean free path, is actually compensated by the use of a shorter tube made of a higher-Z material (gold of higher albedo than copper) so that the radiation temperature drop along the tubes is eventually the same for these two similar shots.

ACKNOWLEDGMENTS

We acknowledge the support of experimental and target preparation staff of the Laser Mégajoule facility and staff of CEA/Valduc for target fabrication.

DATA AVAILABILITY

The data that support the findings of this study are available from the corresponding author upon reasonable request.

Author Contributions

Cedric Courtois: Conceptualization (equal); Formal analysis (equal); Investigation (equal); Methodology (equal); Validation (equal); Visualization (equal); Writing – original draft (equal); Writing –review & editing (equal). **Remy Gisbert:** Conceptualization (equal); Formal analysis (equal); Investigation (equal); Methodology (equal); Validation (equal); Visualization (equal); Writing – original draft (equal); Writing – review & editing (equal). **Ronan Botrel**: Investigation (equal); Resources (equal); Writing – review & editing (equal). **Annaig Chaleil**: Formal analysis (equal); Investigation (equal); Resources (equal); Validation (equal); Writing – review & editing (equal). **Ludovic Chopineau**: Formal analysis (equal); Investigation (equal); Resources (equal); Validation (equal); Writing – review & editing (equal). **Serge Debesset:** Investigation (equal); Ressources (equal); Validation (equal); Writing – review & editing (equal). **Julien Fariaut:** Formal analysis (equal); Investigation (equal); Resources (equal); Validation (equal); Writing – review & editing (equal). **Olivier Henry:** Formal

analysis (equal); Investigation (equal); Validation (equal); Writing – review & editing (equal). **Laurent Le Deroff:** Formal analysis (equal); Investigation (equal); Validation (equal); Writing – review & editing (equal). **Berenice Loupias:** Conceptualization (equal); Formal analysis (equal); Investigation (equal); Methodology (equal); Writing – review & editing (equal). **Adrien Rousseau**: Formal analysis (equal); Investigation (equal); Resources (equal); Validation (equal); Writing – review & editing (equal). **Gerard Soullie:** Formal analysis (equal); Investigation (equal); Resources (equal); Validation (equal); Writing – review & editing (equal). **Bruno Villette:** Formal analysis (equal); Investigation (equal); Resources (equal); Validation (equal); Writing – review & editing (equal).

References

[1]D. Mihalas and B. W. Mihalas, Foundations of Radiation Hydrodynamics (Oxford University Press, New York, 1984).

[2]D. R. Ballantyne, and J. E. Everett, AjJ (2005, ApJ, 626, 364).

[3]V. Tranchant, N. Charpentier, L. Van Box Som, A. Ciardi, and E. Falize, Astrophys. J. 936, 14 (2022).

[4]R. E. Olson, L. J. Suter, J. L. Kline, D. A. Callahan, M. D. Rosen, S. N. Dixit, O. L. Landen, N. B. Meezan, J. D. Moody, C. A. Thomas, A. Warrick, K. Widmann, E. A. Williams, and S. H. Glenzer, Phys. Plasmas 19, 053301 (2012).

[5]D. R. P. Drake, High Energy Density Laboratory Astrophysics, Fundamentals, Inertial Fusion, and Experimental Astrophysics, Springer (2005).

[6]R. E. Marshak, The Physics of Fluids 1, 24 (1958).

[7]O. A. Hurricane and J. H. Hammer, Phys. Plasmas 13, 113303 (2006).

[8]A.P. Cohen, G. Malamud, and S.I. Heizler1, Phys. Rev. Research 2, 023007 (2020).

[9]J.H. Hammer and M. D. Rosen, Phys. Plasmas 10, 1829, (2003).

[10]J. Garnier, G. Malinié, Y. Saillard, and C. Cherfils-Clérouin, Phys. Plasmas 13, 092703 (2006).

[11]D. Hoarty, O. Willi, L. Barringer, C. Vickers, W. Nazarov, Phys. Plasmas 6, 2171(1999).

[12]C. Courtois, C. Robert, D. Bretheau, J. Fariaut, M. Ferri, I. Geoffray, G. Legay, F. Philippe, R. Rosch, G. Soullie, and B. Villette, Phys. Plasmas 28, 073301 (2021).

[13]E. Malka and S. I. Heizler, Phys. Fluids 34, 066105 (2022).

[14]T. Afshar-rad, M. Desselberger, M. Dunne, J. Edwards, J. M. Foster, D. Hoarty, W. Jones, S. J. Rose, P. A. Rosen, R. Taylor, and O. Willi, Phys. Rev. Lett. 73, 74 (1994).

[15]D. Hoarty, L. Barringer, C. Vickers, O. Willi, and W. Nazarov, Phys. Rev. Lett. 82, 3070 (1999).

[16]O. Willi, L. Barringer, C. Vickers, and D. J. Hoarty, Astrophys. J., Suppl. 127, 527 (2000).

[17]J. M. Taccetti, P. A. Keiter, N. Lanier, K. Mussack, K. Belle, and G. R. Magelssen, Rev. Sci. Instrum. 83, 023506 (2012).

[18]H.M. Johns, C.L. Fryer, S.R. Wood, C.J. Fontes, P.M. Kozlowski , N.E. Lanier, A. Liao, T.S. Perry, J.W. Morton, C.R.D. Brown, D.W. Schmidt, T. Cardenas, T.J. Urbatsch, P. Hakel, J. Colgan, S. Coffing, J. Cowan, D. Capelli, L.A. Goodwin, T.E. Quintana, C. Hamilton, F. Fierro, C. Wilson, R.B. Randolph, P. Donovan, T. Sedillo, R. Gonzales, M.E. Sherrill, M.R. Douglas, W.J. Garbett, J.D. Hager, J. Kline, High Energy Density Phys. 39 100939 (2021).

[19]S. X. Coffing, C. L. Fryer, H. F. Robey, C. J. Fontes, S. R. Wood, P. M. Kozlowski, H. M. Johns, D. D. Meyerhofer, T. Byvank, A. Liao, and T. J. Urbatsch, Phys. Plasmas 29, 083302 (2022).

[20]J. Massen, G. D. Tsakiris, K. Eidmann, I. B. Foldes, Th. Lower, R. Sigel, S. Witkowski, H. Nishimura, T. Endo, H. Shiraga, M. Takagi, Y. Kato and S. Nakai, Phys. Rev. E 50, 5130 (1994).

[21]C. A. Back, J. D. Bauer, J. H. Hammer, B. F. Lasinski, R. E. Turner, P. W. Rambo, O. L. Landen, L. J. Suter, M. D. Rosen, and W. W. Hsing, Phys. Plasmas 7, 2126 (2000); C. A. Back, J. D. Bauer, O. L. Landen, R. E. Turner, B. F. Lasinski, J. H. Hammer, M. D. Rosen, L. J. Suter, and W. H. Hsing, Phys. Rev. Lett. 84, 274 (2000).

[22]Y. Xu, S. Jiang, D. Lai, W. Pei, Y. Ding, T. Chang, K. Lan, S. Li, and T. Feng, Laser Part. Beams 24, 495 (2006).

[23]P. A. Rosen, J. M. Foster, M. J. Taylor, P. A. Keiter, C. C. Smith, J. R. Finke, M. Gunderson, T. S. Perry, Astrophys Space Sci 307, 213 (2007)

[24]P. Keiter, M. Gunderson, J. Foster, P. Rosen, A. Comley, M. Taylor, and T. Perry, Phys. Plasmas 15, 056901 (2008).

[25]A. S. Moore, T. M. Guymer, J. Morton, B. Williams, J. L. Kline, N. Bazin, C. Bentley, S. Allan, K. Brent, A. J. Comley, K. Flippo, J. Cowan, J. M. Taccetti, K. Mussack-Tamashiro, D. W. Schmidt, C. E. Hamilton, K. Obrey, N. E. Lanier, J. B. Workman, and R. M. Stevenson, J. Quant. Spectrosc. Radiat. Transfer 159, 19 (2015).

[26]C. Courtois, R. Gisbert, O. Breton, S. Darbon, J. Fariaut, O. Henry, D. Raffestin, C. Reverdin, G. Soullie, and B. Villette, Phys. Plasmas 29, 123301 (2022).

[27]J.L Miquel and E. Prene, Nucl. Fusion 59, 032005 (2019).

[28]J. L. Bourgade, B. Villette, J.L. Bocher, J.Y. Boutin, S. Chiche, N. Dague, D. Gontier, J. P. Jadaud, B. Savale and R. Wrobel, Rev. Sci. Instrum. 72, 1173 (2001). J. L. Bourgade, V. Allouche, J. Baggio, C. Bayer, F. Bonneau, C. Chollet, S. Darbon, L. Disdier, D. Gontier, M. Houry, H. P. Jacquet, J. P. Jadaud, J. L. Leray, I. Masclet-Gobin, J. P. Negre, J. Raimbourg, B. Villette, I. Bertron, J. M. Chevalier, J. M. Favier, J. Gazave, J. C. Gomme, F. Malaise, J. P. Seaux, V. Yu Glebov, P. Jaanimagi, C. Stoeckl, T. C. Sangster, G. Pien, R. A. Lerche, and E. R. Hodgson, Rev. Sci. Instrum. 75, 4204 (2004). J. P. Le Breton, E. Alozy, J. Y. Boutin, A. Duval, S. Gary, D. Gontier, S. Jasmin, M. Naudy, C. Reverdin, R. Rosch, S. Schmitt, G. Soullie, P. Stemmler, B. Villette, R. Wrobel, S. Hulin, C. Meyer, and P. Romary, Rev. Sci. Instrum. 77, 10F530 (2006).

[29]E. Garelis and T. E. Wainwright, Phys. Fluids 16, 476 (1973).

[30]S. T. Bennion. (1971). A method of solution for hydrodynamics and radiation diffusion as a multi-material problem in one dimension. 1-110. UTEC-CSc-71-114.

[31]G. Mishra, K. Ghosh , A. Ray and N.K. Gupta, High Energy Density Physics 27, 1 (2018).

[32]M. D. Rosen, "Marshak Waves: Constant Flux vs. Constant T – a (slight) Paradigm Shift », Lawrence Livermore National Laboratory, Livermore CA, Report No. UCRL-ID-119548, 1994.

[33]T. Shussman1, and S. I. Heizler, Phys. Plasmas 22, 082109 (2015).

[34]J. L. Kline, S. A. Yi, A. N. Simakov, R. E. Olson, D. C. Wilson, G. A. Kyrala, T. S. Perry, S. H. Batha, A. B. Zylstra, E. L. Dewald, R. Tommasini, J. E. Ralph, D. J. Strozzi, A. G. MacPhee, D. A. Callahan, D. E. Hinkel, O. A. Hurricane, J. L. Milovich, J. R. Rygg, S. F. Khan, S. W. Haan, P. M. Celliers, D. S. Clark, B. A. Hammel, B. Kozioziemski, M. B. Schneider, M. M. Marinak, H. G. Rinderknecht, H. F. Robey, J. D. Salmonson, P. K. Patel, T. Ma, M. J. Edwards, M. Stadermann, S. Baxamusa, C. Alford, M. Wang, A. Nikroo, N. Rice, D. Hoover, K. P. Youngblood, H. Xu, H. Huang, and H. Sio, Phys. Plasmas 23, 056310 (2016).

[35]C. Courtois, O. Poujade, E. Alozy, S. Brygoo, C. Chicanne, T. Chies, S. Darbon, A. Duval, J. Fariaut, M. Ferri, H. Graillot, O. Henry, B. Marchet, I. Masclet-Gobin, P. Seytor, G. Soullie, L. Videau, B. Villette, and R. Wrobel, Phys. Plasmas 27, 042702 (2020).

[36]K.W. McLean and S.J. Rose, *JQSRT*, 280, 108070, (2022).

[37]C-J Xiao, G-W Meng and Y-K Zhao, Matter Radiat. Extremes 8, 026901 (2023).

[38]A. P. Cohen and S. I. Heizler, J. Comput. Theor. Transp. 47, 378 (2018).

[39]G. D. Tsakiris, and K. Eidmann, J. Quant. Spectrosc. Radiat. Transfer 38, 353, 1987.

[40]M. Krief and R. G. McClarren, Phys. Fluids 36, 056129 (2024).

[41]Private communication.

[42]E. Lefebvre, S. Bernard, C. Esnault, P. Gauthier, A. Grisollet, P. Hoch, L. Jacquet, G. Kluth, S. Laffite, S. Liberatore, I. Marmajou, P.-E. Masson-Laborde, O. Morice and J.-L. Willien, Nucl. Fusion 59, 032010 (2019).

[43]F.J.D. Serduke, E. Minguez, Minguez, S.J. Davidson, C. A. Iglesias, JQSRT 65, 527 (2000).

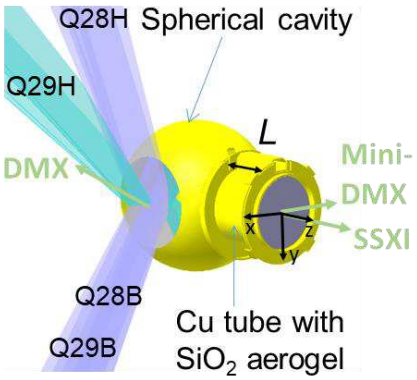

Courtois – Figure 1

Courtois – Figure 2

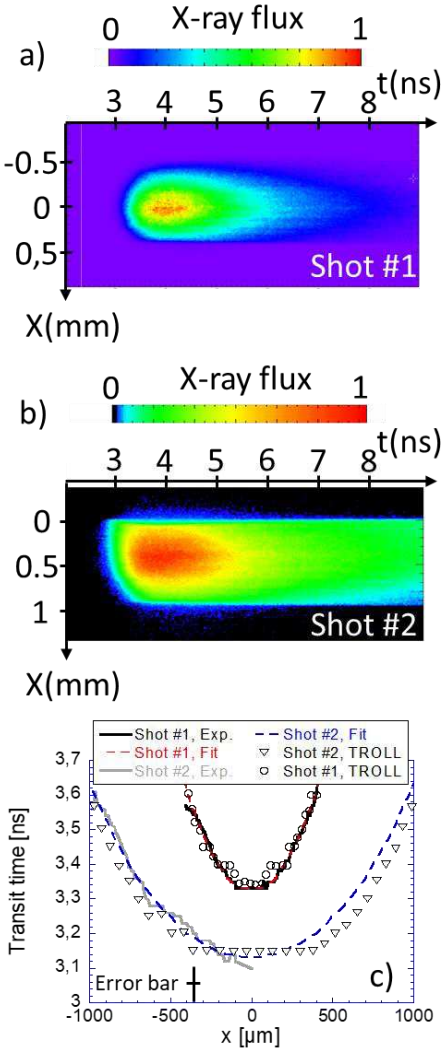

Courtois – Figure 3

Courtois – Figure 4

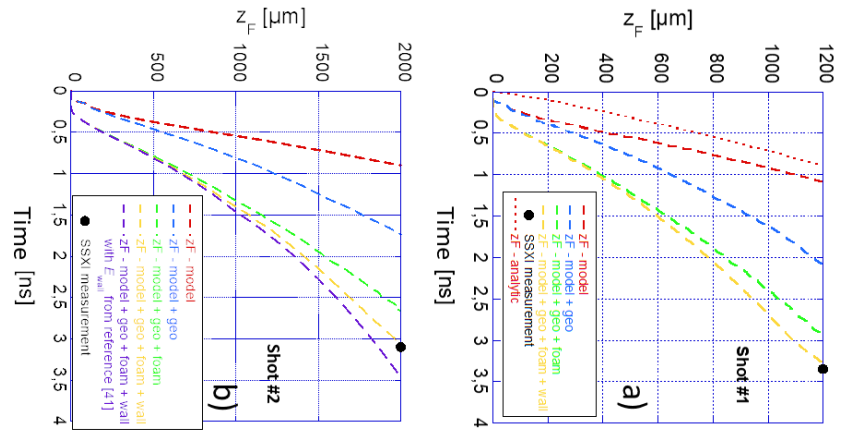

Courtois – Figure 5

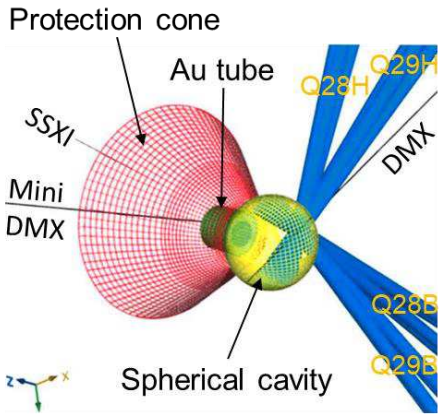

Courtois – Figure 6

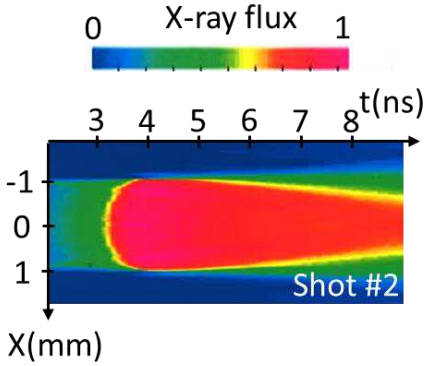

Courtois – Figure 7

PLEASE CITE THIS ARTICLE AS DOI: 10.1063/5.0216671

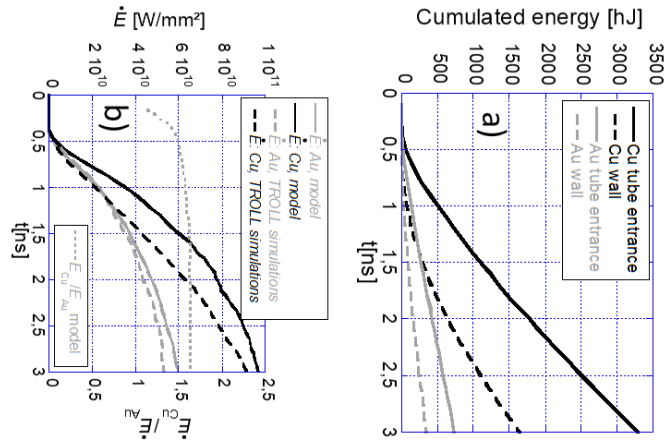

Courtois – Figure 8